Implementation of a Shack-Hartmann Wavefront Sensor for the measurement of embryo induced aberrations using fluorescent microscopy

Oscar Azucena,[1] Joel Kubby,[1] Justin Crest,[2] Jian Cao,[2] William Sullivan,[2] Peter Kner,[3] Donald Gavel,[4] Daren Dillon,[4] Scot Olivier[5]
[1]Jack Baskin School of Engineering, Univ. of California, Santa Cruz, 1156 High St., Santa Cruz, CA 95064, USA
[2]Molecular, Cell, and Developmental Biology, Univ. of California, Santa Cruz, 1156 High St., CA 95064, USA
[3] Department of Biochemistry and Biophysics, University of California, San Francisco, 600-16th St., Box 2240, CA 94158, USA
[4]Laboratory for Adaptive Optics, University of California, 1156 High St., Santa Cruz CA 95064, USA
[5]Physics and Advanced Technologies, Lawrence Livermore National Laboratory, 7000 East Avenue, Livermore, CA 94550, USA

ABSTRACT

Adaptive optics (AO) improves the quality of astronomical imaging systems by using real time measurement of the turbulent medium in the optical path using a guide star (natural or artificial) as a point source reference beacon. AO has also been applied to vision science to improve the current view of the human eye. This paper will address our current research focused on the improvement of fluorescent microscopy for biological imaging utilizing current AO technology. A Shack-Hartmann wavefront sensor (SHWS) was used to measure the aberration introduced by a Drosophila Melanogaster embryo with an implanted 1 micron fluorescent bead that serves as a point source reference beacon. The measurements show an average peak-to-valley and root-mean-square (RMS) wavefront error of 0.77 micrometers and 0.15 micrometers, respectively. The Zernike coefficients have been measured for these aberrations which indicate that the correction of the first 14 Zernike coefficients should be sufficient to correct the aberrations we have obtained. These results support the utilization of SHWS for biological imaging applications and that a MEMS deformable mirror with 1 micron of stroke and 100 actuators will be sufficient to correct these aberrations. The design, assembly and initial results for the use of a MEMS deformable mirror, SHWS and implanted fluorescent reference beacon for wavefront correction will also be discussed.

Keywords: Shack-Hartmann Wavefront Sensor, fluorescent microscopy, biological imaging, Adaptive Optics, Drosophila Melanogaster

1. INTRODUCTION

Changes in the index of refraction due to tissue composition limit the resolving power of biological microscopy [1-4]. This effect is more pronounced in deep tissue imaging where the light travels through many layers of cellular structures including cytoplasm and the plasma membrane. Many important biological processes occur in deep tissue such as stem cell division, neurogenesis and the key developmental events following fertilization [5]. A method that can be used to improve deep tissue imaging is Adaptive Optics (AO). AO is a technique used in telescopes to measure and correct the aberration introduced by turbulence in the optical path [6, 7]. AO has also been applied to vision science to enhance our understanding of the human eye [8, 9].

The idea for using adaptive optics for microscopes is relatively new and a lot of work is still needed [10]. Most adaptive optics microscope systems so far have not directly measured the wavefront due to the complexity of adding a wavefront sensor in an optical system and the lack of a natural point-source reference such as the "guide-star" used in astronomy and vision science. Instead, most AO scanning microscopy systems have corrected the wavefront by optimizing a signal received at a photo-detector by using a hill-climbing algorithm [10]. While there is a lot of important research being

done in AO microscopy, many of the AO systems are specific to each microscope and a universal method for measuring the wavefront (or the results of the correction algorithm) is not currently available. Marcus Feierabend et al., developed a method of obtaining wavefront measurements in highly scattering samples by using a short pulse of light [11]. The length of the pulse served to distinguished scattered light coming from focus by using a coherence gating technique. This method produces good measurements but it requires a very expensive short pulse laser. Booth described some of the difficulties associated with the utilization of a Shack-Hartmann wavefront sensor (SHWS) in AO microscopy [10]. Most of these difficulties can be overcome if a suitable fluorescent point source could be found. Haro et al. developed a technique that utilized the natural fluorescence of lipofuscin to form an incoherent pointlike source for conventional Shack-Hartmann sensing [12]. Beverage, Shack, and Descour used a fluorescent microsphere to measure the three dimensional point spread function of a 40X objective by measuring the wavefront at the aperture of the objective [13]. A method for measuring the wavefront aberrations induced by a *Drosophila* embryo by using a Shack-Hartmann wavefront sensor and light emitted from an imbedded florescent microsphere will be presented. The Drosophila embryo is well suited to analysis as it is approximately 200 μm in diameter, rich in cytoplasm and amenable to experimental manipulation.

2. METHODS

Figure 1 shows the design of the system used to measure the wavefront aberration introduced by the drosophila embryo. Two different objectives 20X and 40X (Melles Griot, Rochester, NY) were used with a numerical aperture of 0.4 and 0.65 respectively. L1 and L2 are 65 mm focal length lenses that image the aperture of the objective (plane P1) onto the Hartmann sensor (plane P2). The field-stop between L1 and L2 blocks the light coming from other microspheres in the field of view, allowing only the light from one microsphere to pass. Note, the field-stop could be moved further down the system since it is only needed by the Hartmann sensor. The minimum size of the field stop was set to 1 mm in image space to prevent spatial filtering of the wavefront. The large distance between L1 and the aperture (P1) allows for the excitation laser (HeNe λ=632nm) to be placed in this area. The laser is directed to the optical path via the 45˚ beam splitter BS1 (Semrock, Rochester, NY). An emission filter was also added after L2 to reduce the effect of scattered laser light by the embryo and allow for the Hartmann Sensor to only see the emission light. By using the 90/10 beam splitter the microsphere can be simultaneously imaged by the Hartmann sensor and the science camera. Immediately following the beam splitter is the wavefront sensor which is composed of a lenslet (AOA Inc., Cambridge, MA) array and a cooled camera (Roper Scientific, Acton, NJ). The lenslet array has 14432 (44x44) lenses , each with a focal length of 24 mm and diameter d_{LA} of 328 μm . The lens L3 demagnifies the pupil by a factor 2 so that it can fit into the cooled camera.

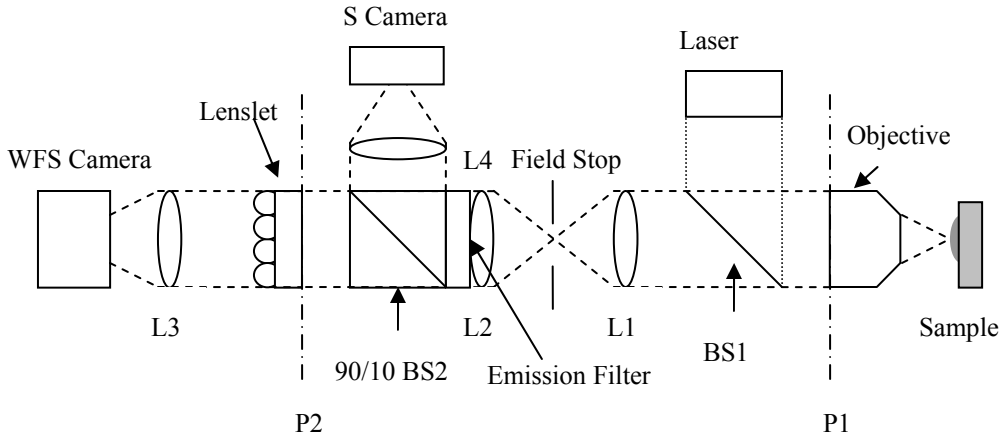

Fig. 1. Microscope set up with a Shack-Hartmann wavefront sensor. BS1 allows the laser light to be focused onto the sample. BS2 allows for both the science camera and the WFS to simultaneously see the fluorescent microsphere.

An important part of measuring an accurate wavefront is the reference source. Astronomical adaptive optics makes use of a laser to create an artificial guide star in the mesospheric sodium layer, 90 km above sea level, which is bright enough to perform adequate wavefront measurements [7]. Powerful and expensive lasers are needed to do so, but the end result is that the adaptive optics system can correct over a much larger portion of the sky relative to the use of "natural

guide stars". The reference source used to measure the wavefront in our AO microscope setup is a crimson fluorescent microsphere that is 1 μm in diameter (Invitrogen, Carlsbad, CA) [14]. Figure 2 shows the general absorption and emission curves of the crimson bead, as well as the excitation source at ~633 nm and the edge of the emission filter at 641 nm (90% pass for wavelengths greater then 641 nm). Note, the peak emission and adsorption of the microspheres are much further away from the emission and absorption of the specimen's Green Fluorescent Protein (GFP) thus preventing photobleaching of the specimen due to the microspheres.

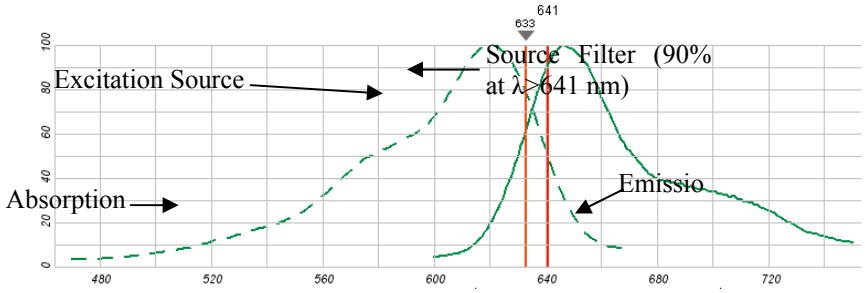

Fig. 2. The absorption and emission curves are shown by the dashed and solid lines, respectively. The edge of the source filter is the red line. The emission filer has a 90% transmission for wavelengths greater then 641 nm.

Embryos from the Oregon-R wild-type strain of *D. melanogaster* were collected for 2 hours on grape juice agar plates at 22°C. These embryos were dechorinated in a 50% bleach solution and transferred to a vial containing 1mL of phosphate-buffered saline (PBS) and 1mL of heptane. Embryos were left at the interface for 45 seconds before addition of 2mL of a formaldehyde solution consisting of 4 parts 37.5% formalin and 5 parts methanol-free 40% para-formaldehyde. These embryos were left in fixative for 25 minutes, at which time all fixative is removed and the embryos are hand devittelinized and stored in PBTA (1x PBS, 1% Bovine Serum Albumin (BSA), 0.05% Triton X-100, 0.02% Sodium Azide) [15].

Glass slides were prepared by adding three spacers of double-sided tape. Dilutions of fluorescent beads (1:5000 and 1:10000) were dropped onto the slide between spacers and allowed to dry for 10min. Fixed embryos were rinsed in PBS and then covered in a glycerol-based mounting media (Vectashield, Vector Laboratories). Embryos were then transferred to the bead-covered areas of the slide followed by a coverslip, which was sealed with nail polish.

3. RESULTS

A reference Hartmann sensor image was obtained to cancel the aberrations introduced by the optical set up, coverslip, and mounting media. The reference image was taken by imaging a single fluorescent bead onto the Hartman sensor. The bead was dried onto a glass slide and imaged with the coverslip and mounting media. The image was processed to obtain the location of the Hartmann spots by using a cross-correlation centroiding algorithm [16]. For each wavefront measurement, a new Hartmann sensor image was acquired with the sample prepared as describe in the previous section. The new measurement was then processed to determine the displacement of the Hartmann spots (slope measurements) relative to the reference image described above. The slope measurements were finally processed to obtain the wavefront by using a Fast Fourier Transform (FFT) reconstruction algorithm [17]. For each measurement the Peak-to-Valley (PV) and the Root-Mean-Square (RMS) wavefront errors were collected. The wavefront function was also expanded into Zernike's circle polynomials to determine the relative strength of the different modes [18]. The Zernike polynomials are normalized and indexed as described by Jason Porter et al. [18]. The wavefront measurements were also used to analyze the point spread function (PSF) by taking the Fourier transform of the complex pupil function:

$$PSF(x,y) = \frac{\left| FT\left\{ P(x',y') * \exp\left(i\frac{2\pi}{\lambda} w(x',y') \right) \right\} \right|^2}{\left| FT\{P(x',y')\} \right|^2_{\xi=0,\eta=0}} \qquad \xi=\frac{x}{\lambda f},\eta=\frac{y}{\lambda f} \tag{1}$$

Where P is one inside the pupil and zero everywhere else, x' and y' are the coordinates at the pupil plane, ξ and η are the spatial frequency in the transform domain, x and y are the coordinates at the image plane, w is the wavefront measurement, λ is the wavelength at which the measurement were taken, and f is the focal length of the lens L2.

A measurement of the wavefront for a 20X objective with a numerical aperture of 0.4 and a limiting aperture of 5.9 mm is shown in Figure 3. The distance between points is equal to the sub-aperture diameter $d_{LA.}$, for a total of 216 apertures on the pupil. As can be seen from Figure 3 the peak to valley wavefront error is ~ 0.56 μm and the RMS wavefront error for this measurement is 0.09 μm. Figure 4 shows the Zernike coefficient for the wavefront shown in Figure 3. As can be seen from Figures 3 and 4, astigmatism and other spherical aberrations dominate the wavefront. This is mainly due to the index mismatches in the optical path as well as the curved body of the embryo, which mostly introduced lower-order aberrations. Note that the optical aberrations due to the coverslip and air glass interface have been removed by the reference image. A reassuring sign shown in Figure 4 is that the amplitude of the higher-order aberrations are decreasing and by correcting a finite number of Zernike modes the imaging qualities of the optical system will improve.

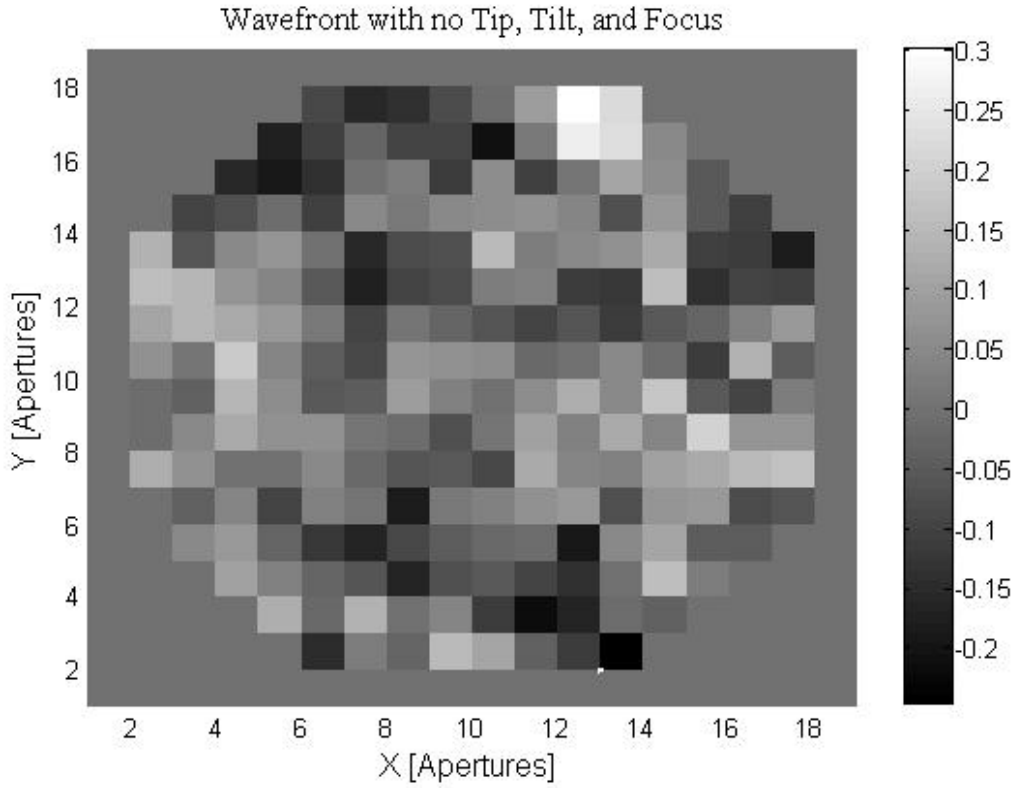

Fig. 3. 20X wavefront measurement with no tip and tilt. The x and y axis are scaled to the sub-aperture diameter. The gray scale legend is in microns.

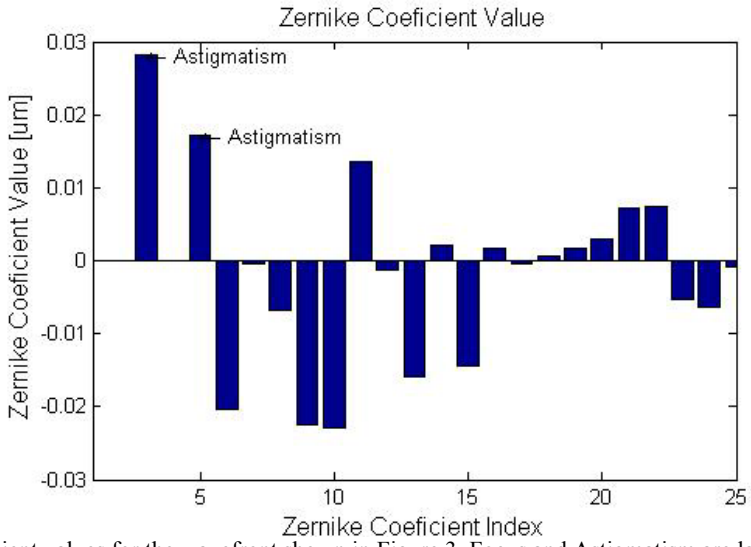

Fig. 4. Zernike coefficient values for the wavefront shown in Figure 3. Focus and Astigmatism are labeled.

Image (a) in Figure 5 shows the PSF for an optical system with no aberrations. Image (b) in Figure 5 displays the PSF calculated by using equation 1 and the wavefront in Figure 3. The Strehl ratio is defined as the ratio of the peak intensity of the PSF relative to the peak intensity of diffraction limited PSF [18]. Image (e) in Figure 5 shows that the Strehl ratio of an uncorrected PSF is approximately 0.37. The effect of removing the first 14 Zernike's can be seen in image (c) and (f) in Figure 5. Using this simulation we can estimate that correcting the first 14 Zernike's will improve the Strehl ratio to 0.70.

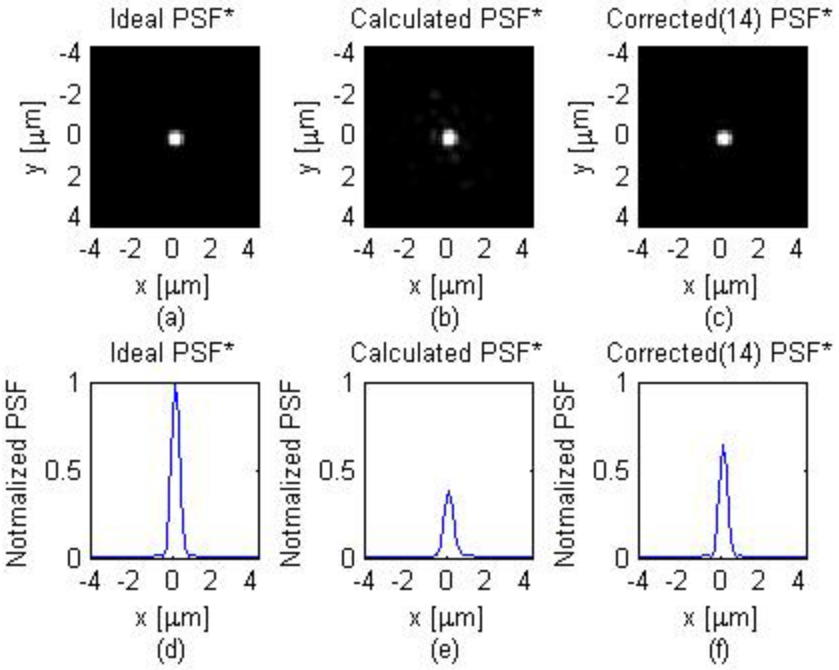

Fig. 5. PSF analysis, (a) calculated using a flat wavefront, (b) calculated using the wavefront in Figure 3 (normalized to its maximum), (c) calculated by removing the first 14 Zernike's of Figure 3, (d) cross-sectional view of (a), (e) cross-sectional view of (b), (f) cross-sectional view of (c).

Table 1 shows the statistical data gathered from the measurements taken. Measurements 1-9 were taken with the 20X objective, measurements 10-15, in gray highlights, were taken with the 40X objective. The measurements show a maximum peak-to-valley (PV) wavefront error of 0.8 µm and 1.3 µm for the 20X and 40X respectively. The maximum

RMS wavefront error was 0.13 μm and 0.19 μm for the 20X and 40X respectively. The higher PV and RMS measurement in the 40X objective are mainly due to the spherical aberrations introduced by the higher numerical aperture. Column four in Table 1 also shows the Strehl ratio obtained by finding the maximum of the PSF image for each measurement. By removing different Zernike modes we can also approximate the effect of removing different amounts of wavefront error. Column five demonstrates the effect of removing the first 14 Zernike's modes from each measurement. The data shows that correcting a small number of modes improves the imaging capabilities of the system.

Table 1. Statistical data for 20X and 40X objectives. Peak-to-Valley (PV), Root-Mean-Square (RMS), Strelh (S), Strehl after correcting first 14 Zernike's (S(14)).

	PV [um]	RMS [um]	S	S(14)
1	0.595	0.092	0.267	0.595
2	0.496	0.076	0.417	0.672
3	0.876	0.127	0.110	0.593
4	0.504	0.063	0.568	0.722
5	0.853	0.097	0.314	0.627
6	0.568	0.076	0.485	0.734
7	0.878	0.127	0.180	0.627
8	0.565	0.081	0.374	0.695
9	0.506	0.089	0.286	0.726
10	0.624	0.089	0.325	0.539
11	0.627	0.076	0.457	0.664
12	0.568	0.089	0.290	0.675
13	1.371	0.161	0.051	0.285
14	1.150	0.189	0.132	0.389
15	1.299	0.132	0.169	0.415
Mean	0.765	0.104	0.295	0.597

Figure 6 shows the statistical data for each Zernike mode for the measurements shown in Table 1. The data shows a gradual decrease in value with increasing Zernike mode. From this we can verify that spherical aberrations are the main source of wavefront error and the aberrations are higher in the 40X objective.

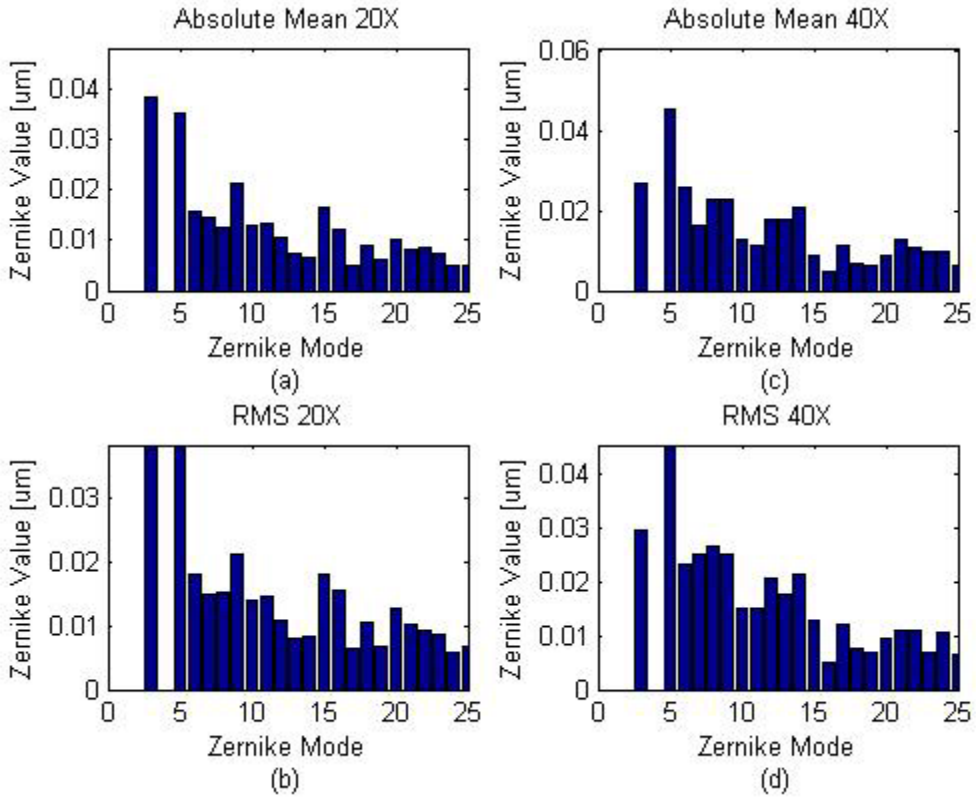

Fig. 6. Zernike statistical data for the measurement in Table 1. (a) and (c) mean of the absolute value for each Zernike mode 20X and 40X respectively, (b) and d) room-mean-square value for each Zernike mode 20X and 40X respectively.

The isoplanatic angle is a relative measure of the field of view over which the AO system can operate and is mathematically defined as [7]:

$$\sigma_\theta{}^2 = \left\langle \left(\phi(X,0) - \phi(X,\theta_0)\right)^2 \right\rangle = 1\, rad^2 \tag{2}$$

Where φ is the wavefront in radians, **X** is a vector representing the two dimensional coordinates, θ_0 is the isoplanatic angle, and $\sigma_\theta{}^2$ is the mean-square error between the measured and observed wavefront. We can determine the isoplanatic half-width by multiplying the isoplanatic angle by the focal length of the objective.

In order to determine the isoplanatic angle we took wavefront measurements from two microspheres separated by a distance *d*. A microsphere was excited by shinning a laser on it. Each microsphere was excited individually. Table 2 shows three different measurements taken with a 40X objective. The first measurement shows that the wavefront error for the bead located at the center of the field of view RMS(1) is 0.98 radians, the wavefront error for the bead located 18 μm from the center RMS is (2) 1.24 radians, and the wavefront error between the two measurements RMS(1-2) is 0.77 radians. Taking the average of three measurements shows the isoplanatic half width is ~ 19 μm.

Table 2. Isoplanatic measurements for the 40X objective using fluorescent microspheres.

Measurement	Distance [μm]	Angle [arcmin]	RMS(1) [rads]	RMS(2) [rads]	RMS(1-2) [rads]
1	18	13.8	0.98	1.24	0.77
2	25	19.1	1.69	1.1	1.3
3	14	10.7	1.6	1.9	0.73
Mean	19	14.5	1.42	1.41	0.93

4. DISCUSSION & CONCLUSIONS

One of the challenges in designing a SHWS is imposed by the amount of light the reference source can provide. Fluorescent microspheres are made out of fluorescent dye and the light emitted is proportional to the radius cubed, thus smaller beads provide less light. The size of the beads should be smaller than the diffraction limit of one subaperture of the Hartmann wavefront sensor. Note that this is larger than the diffraction limit of the microscope aperture by the ratio D(size of the aperture)/d_{LA}(lenslet array diameter). Since the diffraction limit of the microscope is inversely proportional to the numerical aperture (NA) smaller beads are needed for higher numerical aperture systems. Fortunately the light gathered by the objective also increases with increasing NA (light gathering power ~NA^2). Thus increasing the wavefront sampling by a factor of 4, increases the size of the microsphere radius by a factor of 2, and the amount of light emitted by a factor of 8. The only way to determine if a microsphere, or any fluorescent source, will work is to image it into a SHWS using the objective, as shown in Figure 1. In order to increase the speed of the AO loop the bead size should be maximized.

An emerging field in adaptive optics is tomography AO, where multiple reference beacons together with multiple SHWS are used. The information from each wavefront sensor is then processed using a reconstructor to acquire a tomographic image of the changes in the index of refraction in the optical path [7]. One of the advantages of using tomography AO is that it can provide information on the depth dependence variations of the index of refraction in the tissue thus allowing for the AO system to correct for the wavefront aberrations only in the optical path. This technology can also extend the isoplanatic angle by correcting wavefront aberrations that are common to a larger field of view. By depositing multiple fluorescent beads into the biological sample and using multiple wavefront sensors we can also apply the tomographic techniques that have been developed for astronomical AO.

A Shack-Hartmann wavefront sensor was designed to measure the wavefront error induced by a *Drosophila* embryo. The wavefront measurements were taken by using a method of seeding an embryo with a fluorescent microsphere as a "guide star." The maximum wavefront error for a 40X objective was 1.3 μm and 0.19 μm for the peak-to-valley and root-mean-square respectively. The measurements also show that the isoplanatic half width is approximately 19 μm resulting in a field of view of 38 μm in total. Analysis of the data demonstrated that current adaptive optics technology can improve the Strehl ratio of modern microscopes 2 times on average, but improvements as high as 4 times were observed when imaging through 200 μm of tissue.

5. ACKNOWLEDGMENTS

This work has been partially supported by the National Science Foundation Science and Technology Center for Adaptive Optics, managed by the University of California at Santa Cruz under Cooperative Agreement No. AST 9876783 and by the National Science Foundation Science and Technology Center for Biophotonics, managed by the University of California, Davis, under Cooperative Agreement No. PHY 0120999. Oscar Azucena was supported by University of California Systemwide Biotechnology Research & Education Program GREAT Training Grant 2008-19, Jian Cao and Justin Crest were supported by NIH (GM046409), William Sullivan by the California Institute for Quantitative Biosciences (QB3) and Peter Kner by the Center for Biophotonics Science and Technology. We would like to thank Steve Lane and Sebastian Wachsmann-Hogiu from the NSF Center for Biophotonics Science & Technology (CBST) for lending us their camera. We would also like to thank John Sedat from the University of California, San Francisco for his support in this project.

REFERENCES

1. Van Helden, A., *The Invention of the Telescope*, Trans. Am. Phil. Soc. **67**, no. 4., pp. 20-21 (1977).
2. A. Dunn, *Light scattering properties of cells*, Dissertation, University of Texas, Austin http://www.nmr.mgh.harvard.edu/~adunn/papers/dissertation/node7.html, 1998.
3. M. Schwertner, *Specimen-induced distortions in light microscopy*, J. Microscopy **228**, pp. 97-102 (2007).
4. M. Schwertner, M. J. Booth, M. A.A. Neil & T. Wilson, Measurement of specimen-induced aberrations of biological samples using a phase stepping interferometer, **213**, pp. 11-19 (2003).
5. Neil A. Campbell, Jane B. Reece , *Biology*, Benjamin Cummings, San Francisco. 2002.
6. Babcock, H. W., *The possibility of compensating astronomical seeing*, Pub. Astron. Soc. Pac., pp. 229-236 (1953).

7. Hardy, J. W., *Adaptive Optics for Astronomical Telescopes*, Oxford University Press, New York. 1998.
8. Liang J., B. Grim, S. Goelz, and J. F. Bille, *Objective measurement of wave aberrations of the human eye with the use of a Hartmann-Shack wavefront sensor*, J. Opt. Soc. of Am **A, 11**, pp. 1949-1957, (1994).
9. J. Liang, D. R. Williams, D. T. Miller, *Supernormal vision and high-resolution retinal imaging through adaptive optics*, J. Opt. Soc. Am. **A14**, pp. 2884-2892 (1997).
10. M. J. Booth, *Adaptive optics in microscopy*, Phil. Trans. A, Math Phys. Eng. Sci. **365,** pp. 2829-2843 (2007).
11. Marcus Feierabend, Markus Ruckel, and Winfried Denk, *Coherent-gated wavefront sensing in strongly scattering samples*, Opt. Lett., **29,** pp. 2255-2257 (2004).
12. L. D. S. Haro and J. C. Dainty, *Single-pass measurements of the wave-front aberrations of the human eye by use of retinal lipofuscin autofluorescence*, Opt. Lett., **24,** pp. 61-63 (1999).
13. J. L. Beverage, R. V. Shack, and M. R. Descour, *Measurement of the three-dimensional microscope point spread function using a Shack-Hartmann wavefront sensor*, J. Microscopy **205,** pp. 61-75 (2002).
14. Invitrogen Corporation, *Fluorescence SpectraViewer*, http://www.invitrogen.com/site/us/en/home/support/Research-Tools/Fluorescence-SpectraViewer.reg.us.html, Last Accessed: 8/15/2008.
15. Rothwell, W.F., and W. Sullivan, *Fluorescent analysis of Drosophila embryos*. In Drosophila Prot., W. Sullivan, M. Ashburner, and R.S. Hawley, editors. Cold Spring Harbor Lab. Press, Cold Spring Harbor, NY. pp. 141–157 (2000).
16. S. Thomas, T. Fusco, A. Tokovinin, M. Nicolle, V. Michau and G. Rousset, *Comparison of centroid computation algorithms in a Shack-Hartmann sensor*, MNRAS **371**, pp. 323-336 (2006).
17. Lisa A. Poyneer, D. T. Gavel, J. M. Brase, *Fast wave-front reconstruction in large adaptive optics systems with use of the Fourier transform*, J. Opt. Soc. Am. A, **19**(10), pp. 2100-2111 (2003).
18. J. Porter, H. Queener, J. Lin, K. Thorn, A. Awwal, *Adaptive Optics for Vision Science*, Wiley-Interscience, New Jersey, 2006.